Constraints on the amplitude of gravitational wave echoes from black hole ringdown using minimal assumptions

Andrea Miani[1,2,*], Claudia Lazzaro,[3,4] Giovanni Andrea Prodi[5,2] Shubhanshu Tiwari,[6] Marco Drago[7,8]
Edoardo Milotti[9,10] and Gabriele Vedovato[3,4]

[1]*Università di Trento, Dipartimento di Fisica, I-38123 Povo, Trento, Italy*
[2]*INFN, Trento Institute for Fundamental Physics and Applications, I-38123 Povo, Trento, Italy*
[3]*Università di Padova, Dipartimento di Fisica, I-35121 Padova, Italy*
[4]*INFN, Sezione di Padova, I-35131 Padova, Italy*
[5]*Università di Trento, Dipartimento di Matematica, I-38123 Povo, Trento, Italy*
[6]*Physik-Institut, University of Zurich, Winterthurerstrasse 190, 8057 Zurich, Switzerland*
[7]*Università di Roma, Dipartimento di Fisica, I-00133 Roma, Italy*
[8]*INFN, Sezione di Roma, I-00133 Roma, Italy*
[9]*Università di Trieste, Dipartimento di Fisica, I-34127 Trieste, Italy*
[10]*INFN, Sezione di Trieste, I-34127 Trieste, Italy*

Gravitational wave echoes may appear following a compact binary coalescence if the remnant is an "exotic compact object." Exotic compact objects are proposed alternatives to the black holes of Einstein's general relativity theory and are predicted to possess reflective boundaries. This work reports a search for gravitational wave transients (GWTs) of generic morphology occurring shortly after ($\lesssim 1$ s) binary black hole (BBH) mergers, therefore targeting all gravitational wave echo models. We investigated the times after the ringdown for the higher signal-to-noise ratio BBHs within the public catalog GWTC-3 by the LIGO-Virgo-KAGRA collaboration. Our search is based on the coherent WaveBurst pipeline, widely used in generic searches for GWTs by the LIGO-Virgo-KAGRA collaboration, and deploys new methods to enhance its detection performances at low signal-to-noise ratios. We employ Monte Carlo simulations for estimating the detection efficiency of the search and determining the statistical significance of candidates. We find no evidence of previously undetected GWTs and our loudest candidates are morphologically consistent with known instrumental noise disturbances. Finally, we set upper limits on the amplitude of GW echoes for single BBH mergers.

I. INTRODUCTION

The LIGO [1] and Virgo [2] observatories have successfully detected about 90 gravitational wave transients (GWTs) in past observing runs [3–5], all associated to compact binary coalescences (CBCs). More than 90% of these GWTs are identified as generated by the merger of binary black hole (BBH) systems. Recently, this worldwide observatory has expanded to include the KAGRA detector [6]. A new observing run is currently ongoing, and low latency alerts of more CBC GWTs are being publicly released [7]. Investigating the black hole (BH) nature through GW astronomy is therefore a very hot topic in fundamental physics, especially in view of the so-called BH information paradox [8]. The LIGO-Virgo-KAGRA collaboration (LVK) already published several results of tests

of the general relativity theory (GR) [9–13], exploiting the GWTs emitted by BBHs.

Several recent papers [14–25] addressed the topic of exotic compact objects (ECOs) [26]: possible compact objects alternative to the BHs predicted by Albert Einstein's GR theory. Examples of ECOs include wormholes [27], boson stars [28], gravastar [29], and fuzzballs [30]. These ECO models are characterized by different astrophysical properties, like their constituent "matter," but they all share one physical characteristic: Planck-scale modifications of the BH event horizon due to quantum effects [18] or the presence of a surface of different nature [17,31]. This feature would enable the emission of repeated GWTs occurring shortly after the BBH merger time, echoes of the ECO remnant ringdown [14,15,32].

In this work, we report a systematic search for echo signals of generic morphology occurring after the merger-ringdown phase of BBH GWTs [33]. The detection performance of the method is demonstrated down to low signal-to-noise ratios (SNRs), and the results are practically

*Corresponding author.
andrea.miani@unitn.it

064018-1

independent of the echo signal morphology. We also provide upper limits on the strain amplitude at earth of echoes for the loudest BBH GWTs in the LVK catalogs [3–5]. The search is based on the coherent WaveBurst pipeline (cWB) [34–38] widely used to search for generic short duration GWTs by LVK [39–41].

Section II provides a brief review of GW echo models and discusses the main characteristics of the predicted echo signals. In Sec. III we summarize the data analysis method focusing on novel features: in particular, on the search for weak post-merger-ringdown GWTs, the simulations with software signal injections and the construction of the confidence belt on echoes' h_{rss} [42] strain amplitude. Section IV reports the search results including detection performances, checks of robustness to different echo morphologies, and upper limits on the echoes' h_{rss}. A comparative discussion with respect to four, previously published, echo searches [21,23,24,43] is reported in Sec. V. Conclusions are drawn in Sec. VI.

II. GRAVITATIONAL WAVE ECHOES

Distinctive properties of an ECO remnant derives from the dynamics of its inner barrier, interpreted as an effective surface, located above the wouldbe BH event horizon (EH), r_{eh}, [16,17,44] at a radius r_{in} from the object's center

$$r_{in} = r_{eh} + l. \qquad (1)$$

Here, in Eq. (1), l is the length correction to the would be BH EH, and it is theorized to be extremely small [15,17,18], of the order of the Planck length ($l_{Planck} \sim 2 \times 10^{-35}$ m). The inner barrier couples to the outer one (i.e., angular-momentum potential barrier) acting as a sort of cavity [19]. If the remnant compact object of a CBC is not a GR BH; i.e., it is not fully absorbing, the merger-ringdown can trigger multiple outer and inner barrier excitations [14,15]. This results in a train of pulses of outgoing GW radiation of decreasing energy called "echoes" [45,46].

Since the performance of our method is independent to details on the phase evolution of the signal, we can safely test it under the simplifying assumption of a non-rotating ECO remnant.[1] This assumption has also been adopted in many searches in the literature [18–24]. A complete description of a possible echo template for a spinning ECO remnant, as expected from a compact binary coalescence, is provided in [15]. The main parameters

---

[1]According to, e.g., [15], echoes from a spinning remnant show a much larger variety of morphologies, including, e.g., a redshift of the echo central frequency vs pulse order as well as different relative contributions of the + and × GW polarization components at different pulses. However, the sensitivity of our search is invariant when expressed in terms of the h_{rss} component that is detectable by the GW observatory for a given GWT. Of course, the interpretation of our measurement in terms of the source model will be different.
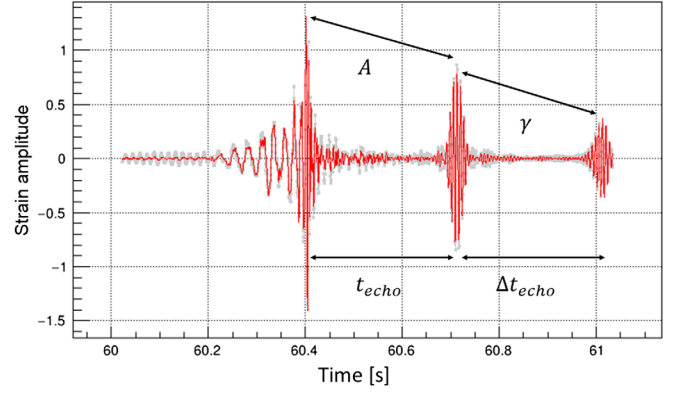

FIG. 1. Simulated inspiral-merger-ringdown-echoes GW transient signal vs time at one detector: the red line is the whitened reconstructed signal strain $h(t)$; the gray line is the whitened data. The CBC signal peaks at the merger time (60.42 s) and is followed by echoes, whose main parameters are visualized.

characterizing the models of echoes are these [21,22] (see also Fig. 1):

(1) Δt_{echo}: the time separation between subsequent pulses as measured by a distant observer. It corresponds to the round-trip travel time of the space-time perturbation between the inner and outer barriers [17].

(2) t_{echo}: the delay of the first echo pulse from the coalescence time of the binary. In general $t_{echo} \sim \Delta t_{echo}$ apart from small effects related to the strong nonlinearity close to the merger time.

(3) γ: the attenuation per round-trip in terms of the GW amplitude ratio between subsequent echo pulses ($0 < \gamma < 1$).

(4) A: amplitude ratio between the amplitude of the first echo and the one at merger time ($0 \leq A < 1$).

Following [16,17], the theoretical prediction for Δt_{echo} is clearly related to the space-time geometry outside the ECO remnant:

$$\Delta t_{echo} \sim 2 \int_{r_{in}}^{r_{out}} \frac{1}{\sqrt{F(r)B(r)}} dr, \qquad (2)$$

where in Eq. (2), $F(r)$ and $1/B(r)^2$ are the coefficients functions for the time and radial component of the metric in a spherically symmetric system, r_{in} is the radius of the inner barrier and r_{out} the radius of the outer barrier. Equation (2) takes into account the effects of gravitational redshift and spatial curvature on the emission of GW echoes. The resulting approximate expression for the time separation is [16,17]

---

[2]The space-time geometry outside an ECO remnant can be described with the $ds^2 = -F(r)dt^2 + 1/B(r)dr^2 + r^2 d\Omega^2$ metric. Such a metric is used to generally describe a static compact object with spherical symmetry and matter localized only in the region $r < r_{shell}$. Following Birkhoff's theorem, in the region $r > r_{shell}$ the Schwarzschild metric holds: $F(r) = B(r) = (1 - \frac{2GM}{c^2 r})$.

$$\Delta t_{\mathrm{echo}} \approx 54 \left(\frac{n}{4}\right) M_{30} \left[1 - 0.001 \ln\left(\frac{l/l_{\mathrm{Planck}}}{M_{30}}\right)\right] \mathrm{ms}. \qquad (3)$$

Here, n is a parameter of the order of the unity that takes into account the structure of the ECO nature [17,20], $M_{30} \equiv M/30 M_{\odot}$ with M standing for the final mass of the remnant. Therefore, a measurement of Δt_{echo} would provide information over the theorized nature of the ECO through the parameters n and l, related to the compactness of the ECO [14]. According to Eq. (3), typical values for echoes time separation are $\Delta t_{\mathrm{echo}} \in (30, 400)$ ms for BBH mergers whose total mass ranges in $\in (10, 100) M_{\odot}$, like most of those detected during O1, O2, and O3 by the LV collaborations [3–5].

A. Signal proxy for echoes

Our detection algorithm does not make use of signal templates, and for testing its performance we can rely on loose signal proxies. The template we selected to mimic echo signals $h_{\mathrm{echo}}(t)$ is a double sine-Gaussian (SGE) pulse $h_{\mathrm{echo}}(t) = h_{\mathrm{SGE}}(t) + \gamma \cdot h_{\mathrm{SGE}}(t - \Delta t_{\mathrm{echo}})$ with $h_{\mathrm{SGE}}(t)$ [47]:

$$h_{+,\mathrm{SGE}}(t) = h_0 \frac{1 + \cos^2(\iota)}{2} e^{-\frac{t^2}{\tau^2}} \sin(2\pi f_0 t + \phi_0),$$

$$h_{\times,\mathrm{SGE}}(t) = h_0 \cos(\iota) e^{-\frac{t^2}{\tau^2}} \cos(2\pi f_0 t + \phi_0), \qquad (4)$$

In Eq. (4), h_0 is the signal amplitude, ι is the inclination angle of the source, τ the half-time duration of the pulse, f_0 and ϕ_0 its central frequency and phase, respectively. The values we select for these parameters are these:

(1) h_0 is defined as $h_0 = A \cdot h_{\mathrm{max}}$, where h_{max} is the GW amplitude at the merger. In our simulations, A is randomly selected per each injection within a uniform distribution $0 < A < 1$ (see Sec. III C).

(2) $\gamma = 0.5$ so that the second echo is contributing $1/3$ of the injected SNR. This is an intermediate condition on the concentration of the signal in time and makes it possible to study the reconstruction of a weaker echo, separately from the first.

(3) $\tau = 20$ ms and $f_0 = 140$ Hz, are close to expectations for the typical mass range of BBH mergers in GWTC-3.

(4) $\phi_0 = 0$. This is not impacting the results since the search method is agnostic on the signal phase in each pulse.

(5) $t_{\mathrm{echo}} = 300$ ms and $\Delta t_{\mathrm{echo}} = 300$ ms are intermediate values for the investigated BBH mergers (see Sec. IV A) according to Eq. (3).

(6) ι is set equal to the one of the injected BBH signal. Furthermore, the sky location of the echo signal proxy is the same as the one of the BBH GWT.

III. SEARCH METHODS

This section describes the methods developed to search for generic GWTs after BBH mergers, such as echo signals. The analysis is based on cWB methods and comprises Monte Carlo simulations to tune the search and interpret the results in terms of gravitational wave echoes. We call this new analysis cWB echo signal (ES) search.

A. Coherent WaveBurst

Coherent WaveBurst [37,38] is a data analysis pipeline searching for generic GWT signals in the data from the LVK GW detectors network [48–50]. Designed to operate without a specific waveform model, cWB first identifies coincident excess power in the multiresolution time-frequency (TF) representations of the detectors' strain data [36]. Then, for the selected events, cWB reconstructs the source sky location and the signal waveform of each GW candidate by means of a constrained maximum likelihood method [35].

To be robust against the non-stationary detector noise cWB employs signal-independent vetoes, reducing the initial high rate of the excess power triggers. The primary selection cut is on the network correlation coefficient c_{c} [34], defined as

$$c_{\mathrm{c}} = \frac{E_{\mathrm{c}}}{E_{\mathrm{c}} + E_{\mathrm{null}}}, \qquad (5)$$

which is informative on the coherence of a signal among the detectors of the network. Here, E_{c} and E_{null} [34,35,51] are the coherent and the null energy of the signal. The algorithm also combines all the data streams into one coherent statistic η_{c} [34], which is used for ranking the detected events and is defined as

$$\eta_{\mathrm{c}} = \sqrt{\frac{c_{\mathrm{c}} \cdot E_{\mathrm{c}}}{N - 1}}, \qquad (6)$$

with N the number of detectors in the network. Typically, for a GW signal $c_{\mathrm{c}} \sim 1$ while for instrumental glitches $c_{\mathrm{c}} \ll 1$. By setting a threshold value on c_{c}, it is possible to reconstruct events with a lower or higher probability of being genuine GW signals.

In the LVK analyses, different cWB searches are used depending on the target GWT. In a previous work, cWB was used to investigate postmerger GW emission in a configuration more sensitive to the chirping morphology of the CBCs signals [52]. Currently, the most general cWB search is the all-sky burst search [39–41], with a proven ability to detect the broadest variety of GW signal morphologies. Our search method is based on this cWB instance, the same version used in the LVK O3 analysis [37,41], thus it is more agnostic than [52]. The following subsections describe the peculiarities of cWB ES search.
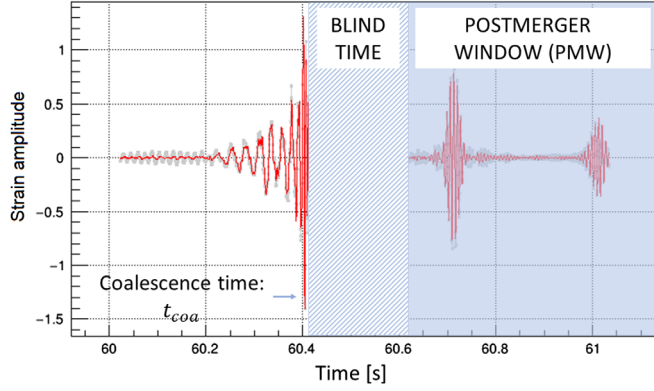
FIG. 2. This plot shows the segmentation of the analyzed time following up an event (red line). The pale blue opaque area is representative of the blind time $\Delta t_{\mathrm{blind}}$, and the light blue transparent area after it highlights the postmerger window.

B. Searching for echoes

Due to the expected nature of echoes, the cWB all-sky burst search is modified to select more TF pixels with a low energy content and scattered over a wider than usual time span (see Appendix A). Triggering and final selection thresholds are decreased, and to group different pulses (i.e., the BBH merger and the echolike signals) into a single event, we increase the maximum time separation between disjoint clusters of pixels which define a single event. Specifically, the η_c threshold is decreased from 5.0 to 3.5, and the T_{gap} parameter [38] is increased up to 2 s. Also, the whitening [53] of the data is performed using a TF map resolution that mitigates the leakage of the merger-ringdown signal of the remnant into the subsequent TF pixels. Indeed, while the cWB all-sky burst search performs the whitening in the TF map with the best frequency resolution, typically $\Delta f = 1$ Hz and $\Delta t = 0.5$ s, here we adopt a better time resolution, using pixels with a time width of $\Delta t = 0.125$ s and $\Delta f = 4$ Hz.

The search uses the BBH GWT as a trigger and focuses on a user-defined postmerger time interval, called a "postmerger window" (PMW), see Fig. 2. The PMW starts at time $t_{\mathrm{start}}^{\mathrm{PMW}}$, defined as

$$t_{\mathrm{start}}^{\mathrm{PMW}} = t_{\mathrm{coa}} + \Delta t_{\mathrm{blind}}, \qquad (7)$$

where t_{coa} is the coalescence time of the BBH system and $\Delta t_{\mathrm{blind}}$ a user-defined blind time. The blind time's purpose is to mask the ringdown of the BBH signal, and its impact on the analysis will be discussed in Sec. IV A. Limiting the ES search to a PMW allows us to limit the noise contribution in the postmerger without penalizing the capability to detect possible echo signals. We adopted two choices of PMW:

(1) for $t_{\mathrm{echo}} \leq 200$ ms we use $\Delta t_{\mathrm{blind}} = 50$ ms and $\Delta t^{\mathrm{PMW}} = 300$ ms and

(2) for $t_{\mathrm{echo}} > 200$ ms we use $\Delta t_{\mathrm{blind}} = 200$ ms and $\Delta t^{\mathrm{PMW}} = 1$ s.

Such choices are suitable to include the first $\sim$1–4 echo pulses according to Eq. (3).

Within the PMW, the main statistical parameters we compute are the network correlation coefficient, c_c^{PMW}, analogous to c_c [see Eq. (5)], and the network signal-to-noise ratio of the data, $\mathrm{SNR}^{\mathrm{PMW}}$, defined as

$$\mathrm{SNR}^{\mathrm{PMW}} = \sqrt{\sum_k^N \sum_{j \in J} (x_k[j])^2}, \qquad (8)$$

where J is the set of the TF pixels corresponding to times inside Δt^{PMW}, and $x_k[j]$ are the whitened reconstructed data.

While cWB can work with arbitrary detectors networks, the ES search deployed here is run only over the two LIGO detectors network (H, Hanford, and L, Livingston [1]). The motivation is twofold. On one side, H and L detect most of the GWTs' SNR. Moreover, under O2 and O3 conditions, the detection performance of minimally modeled searches for GWTs results more effective when restricted to the LIGO network of almost coaligned detectors [41]. This comes from a complex balance between background rejection capabilities against collection of GW information, as the target signal parameter space becomes higher dimensional when searching also Virgo [2] due to the need of taking into account both GW polarization components.

C. Monte Carlo estimators

The ES search follows a two-track scheme: the background (BKG) analysis, and the signal (SIG) analysis. Both analyses are off-source experiments, meaning that the data do not include the times corresponding to the detected GW signals. The ES search is separately performed for each BBH GWT considered.

The BKG analysis is used to estimate the noise statistics for the null hypothesis in the PMW. We create a set of off-source software signal injections over the data stream using waveform templates of the specific BBH event under study. These templates are randomly selected from the CBC waveform posterior samples [54,55], provided by the parameter estimation (PE) methods for the considered GW event (following the approximants used in [3–5]). The signals are injected widely separated, i.e., one each 600 s, to avoid systematic interferences in the analysis.

The SIG analysis enables the measurement of the sensitivity of the ES search to signals within the PMW. The injected BBH GWTs are the same as the BKG analysis with, in addition, the injection of secondary signals after each BBH merger according to the echo model of Sec. II A. Different morphologies of secondary signals have been tested as well, see Sec. IV A.
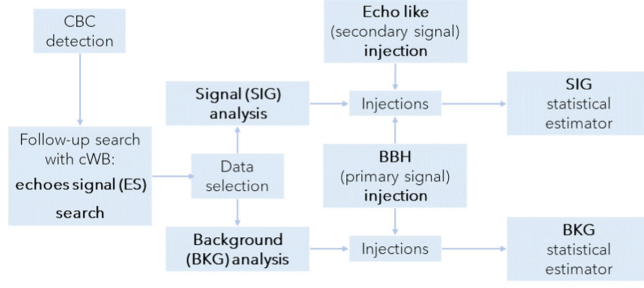
FIG. 3. Flowchart of the ES search. Once the cWB all-sky burst search detects a BBH event, the cWB ES search can be run as a follow-up. The search runs two parallel studies on a common data selection: the background and the signal, and computes all the statistical estimators described in Sec. III B. The BBH primary signal injections are randomly picked from the PE samples distribution for that event.

This double simulation scheme is depicted in Fig. 3. The data used for all studies are real data available at the GW open science center of the LVK collaboration, see [54,55]. These two analyses allow us to study the detection probability, DP, and the false alarm probability, FAP, as functions of the reconstructed $\mathrm{SNR}_{\mathrm{rec}}^{\mathrm{PMW}}$. Their definition is the following:

$$\mathrm{DP} = \frac{\mathrm{EV}_{\mathrm{SIG}}(\mathrm{SNR}_{\mathrm{rec}}^{\mathrm{PMW}} \geq th_{\mathrm{snr}})}{\mathrm{EV}}$$

$$\mathrm{FAP} = \frac{\mathrm{EV}_{\mathrm{BKG}}(\mathrm{SNR}_{\mathrm{rec}}^{\mathrm{PMW}} \geq th_{\mathrm{snr}})}{\mathrm{EV}}, \qquad (9)$$

and here $\mathrm{EV}_{\mathrm{SIG}}$ and $\mathrm{EV}_{\mathrm{BKG}}$ are the number of detected events above threshold in the PMW from the SIG and BKG distributions, EV is the total number of injected signals, and th_{snr} is the threshold value on $\mathrm{SNR}_{\mathrm{rec}}^{\mathrm{PMW}}$.

D. Tuning the analysis internal thresholds

The cWB internal thresholds, described in Sec. III B and listed in Appendix A, are related to the energy content of a possible trigger, its energy per degree of freedom, and its coherence within the detectors' network. On the contrary, they are agnostic to the signal morphology or spectral characterization, so they allow us to address a very wide range of different statistical noise conditions.

The tuning criteria of the internal thresholds are based on the receiver operating characteristics curves, which are built from the DP and FAP measurements. The chosen configuration of the analysis is the one that maximizes the DP for low values of FAP, in the interval $0.5\% \leq \mathrm{FAP} \leq 5\%$. This region corresponds to the events which possess low to medium $\mathrm{SNR}_{\mathrm{rec}}^{\mathrm{PMW}}$, typically $4 \leq \mathrm{SNR}_{\mathrm{rec}}^{\mathrm{PMW}} \leq 8$. The tuning has been extensively performed on the simulations related to the GW150914 event [56–58]. We have checked as well that the same setup is also providing the best results for a few GWTs from O3, including GW190521 [59].

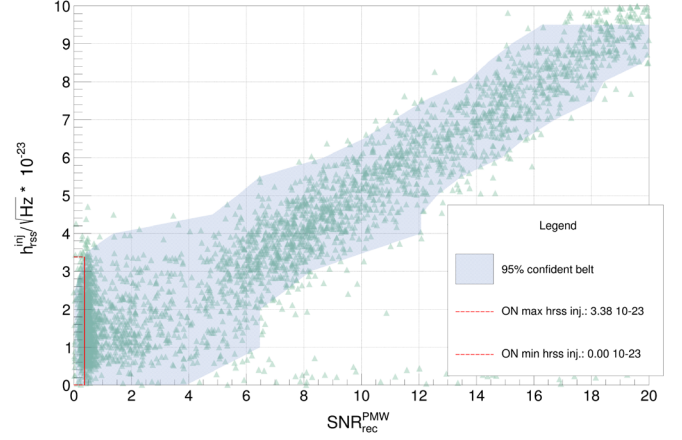The list of tuned parameters is reported in Appendix A.

FIG. 4. Confidence belt for the echo's injected amplitude h_{rss}, $h_{\mathrm{rss}}^{\mathrm{inj}}$, vs the reconstructed $\mathrm{SNR}_{\mathrm{rec}}^{\mathrm{PMW}}$ in the PMW for GW150914. The blue region corresponds to 95% coverage. The on-source 95% confidence interval in terms of the h_{rss} is set by the intersection between the vertical line at the on-source value $\mathrm{SNR}_{\mathrm{ON}}^{\mathrm{PMW}} \sim 0.38$ (red line) and the blue region. The y axis values are in units of $10^{-23}/\sqrt{\mathrm{Hz}}$. The scatter plot shows SIG simulation data points but not BKG ones for readability; 95% of the BKG samples have an $\mathrm{SNR}_{\mathrm{rec}}^{\mathrm{PMW}} \leq 4$.

E. Inference of confidence intervals

Searches for GWTs of generic morphologies, such as cWB ES, directly measure the energy or integrated squared amplitude of the candidate signal. Here, results are presented in terms of h_{rss} [42] at Earth

$$h_{\mathrm{rss}} = \sqrt{\int_{t \in \mathrm{PMW}} (|h_+(t)|^2 + |h_\times(t)|^2) dt} \qquad (10)$$

of signals consistent with the on-source data in the PMW.

The SIG simulations provide estimates of the conditional distributions of the recovered $\mathrm{SNR}_{\mathrm{rec}}^{\mathrm{PMW}}$ as a function of $h_{\mathrm{rss}}^{\mathrm{inj}}$, the h_{rss} of the injected postmerger signal. We use the conditional distributions to build the confidence belts [60] on $h_{\mathrm{rss}}^{\mathrm{inj}}$, as shown in Fig. 4. This is approximately achieved by introducing a binning in $h_{\mathrm{rss}}^{\mathrm{inj}}$ which ensures a minimum number of samples, hundreds per bin, and allows us to target a confidence belt coverage of 95%. The related cost is to perform specific SIG simulations with much higher statistics than those needed for estimating the DP. For the special case of $h_{\mathrm{rss}}^{\mathrm{inj}} = 0$, the null hypothesis, we exploit the full statistics of the BKG simulation. The confidence belt is then used to set the 95% confidence interval on the expected $h_{\mathrm{rss}}^{\mathrm{inj}}$ for signals inside the PMW that posses a $\mathrm{SNR}^{\mathrm{PMW}}$ equal to the one measured on source, $\mathrm{SNR}_{\mathrm{ON}}^{\mathrm{PMW}}$.

IV. RESULTS

Using the search tuning described in Sec. III D, we investigated a subset of 33 BBH events from the BBH

TABLE I.   The analyzed BBH GWTs with $SNR_{net} \geq 10$ in the all-sky cWB search [39–41], listed in chronological order. Columns report the observing run; GWT name; waveform model used in BKG and SIG simulations (1 = IMRPhenomPv2 approximant, 2 = SEOBNRv4PHM approximant, as the one used in [3–5]); GPS coalescence time t_{coa} to ms resolution from the PE waveform posterior information available through GWOSC [54,55]; network SNR as reconstructed by the cWB all-sky search for burst GWTs; h_{rss} in PMW that ensures DP = 50% at FAP = 5%; predicted t_{echo} [following Eq. (3) and assuming $n = 8$, wormhole, and $l/l_{Planck} = 2$]; on-source SNR inside the PMW, SNR_{ON}^{PMW}; p value of SNR_{ON}^{PMW} with statistical uncertainties. The analyzed PMW is [50,350] ms for GWTs with $t_{echo} \leq 200$ ms, [0.2,1.2] s otherwise.

List of analyzed BBH events							
Run - GW name	Approximant	t_{coa}	SNR_{net}	$h_{rss}^{50\%} \cdot \frac{10^{-23}}{\sqrt{Hz}}$	t_{echo} [ms]	SNR_{ON}^{PMW}	p value$_{ON}$
O1 - GW150914	1	1126259462.421	24.4	2.79 ± 0.02	227^{+12}_{-11}	0.4	0.849 ± 0.006
O1 - GW151012	1	1128678900.467	10.0	2.57 ± 0.03	127^{+39}_{-14}	0.1	0.54 ± 0.01
O1 - GW151226	1	1135136350.668	13.1	2.70 ± 0.03	73^{+23}_{-5}	0.2	0.8 ± 0.1
O2 - GW170104	1	1167559936.619	13.0	2.52 ± 0.01	176^{+18}_{-14}	0.4	0.673 ± 0.006
O2 - GW170608	1	1180922494.501	14.9	2.63 ± 0.01	63^{+12}_{-2}	2.2	0.034 ± 0.003
O2 - GW170729	1	1185389807.346	10.2	2.53 ± 0.01	287^{+53}_{-37}	2.5	0.043 ± 0.003
O2 - GW170809	1	1186302519.758	12.4	2.40 ± 0.02	203^{+19}_{-14}	≤ 0.1	0.56 ± 0.02
O2 - GW170814	1	1186741861.533	15.9	2.51 ± 0.02	191^{+12}_{-9}	1.5	0.450 ± 0.007
O2 - GW170823	1	1187529256.501	11.5	2.50 ± 0.02	236^{+36}_{-27}	≤ 0.1	0.835 ± 0.006
O3a - GW190408_181802	2	1238782700.279	14.7	1.82 ± 0.01	147^{+14}_{-10}	1.1	0.155 ± 0.005
O3a - GW190412	2	1239082262.165	18.9	1.82 ± 0.01	134^{+14}_{-14}	1.2	0.273 ± 0.007
O3a - GW190512_180714	2	1241719652.435	12.3	1.69 ± 0.02	123^{+14}_{-12}	≤ 0.1	0.55 ± 0.02
O3a - GW190513_205428	2	1241816086.800	12.3	1.83 ± 0.01	185^{+29}_{-21}	0.2	0.882 ± 0.004
O3a - GW190517_055101	2	1242107479.848	10.2	1.80 ± 0.02	213^{+33}_{-32}	≤ 0.1	0.52 ± 0.01
O3a - GW190519_153544	2	1242315362.418	12.0	1.84 ± 0.01	365^{+45}_{-50}	0.4	0.302 ± 0.006
O3a - GW190521	2	1242442967.471	14.4	1.74 ± 0.01	568^{+133}_{-81}	0.2	0.858 ± 0.004
O3a - GW190521_074359	2	1242459857.456	24.4	1.73 ± 0.01	256^{+23}_{-16}	0.5	0.218 ± 0.006
O3a - GW190602_175927	2	1243533585.093	12.1	1.98 ± 0.04	402^{+64}_{-54}	0.2	0.838 ± 0.005
O3a - GW190701_203306	2	1246048404.578	11.6	1.84 ± 0.01	326^{+41}_{-32}	6.4	0.0019 ± 0.0007
O3a - GW190706_222641	2	1246487219.361	12.3	1.82 ± 0.01	358^{+66}_{-49}	0.3	0.100 ± 0.004
O3a - GW190814	2	1249852257.009	22.2	1.82 ± 0.01	91^{+4}_{-3}	0.5	0.718 ± 0.005
O3a - GW190828_063405	2	1251009263.781	16.0	1.82 ± 0.01	197^{+26}_{-15}	1.0	0.474 ± 0.006
O3a - GW190915_235702	1	1252627040.693	13.1	1.88 ± 0.02	205^{+26}_{-22}	0.2	0.720 ± 0.008
O3a - GW190929_012149	1	1253755327.505	9.9	1.86 ± 0.02	367^{+122}_{-92}	0.1	0.860 ± 0.005
O3b - GW191109_010717	2	1257296855.783	17.3	1.85 ± 0.01	387^{+65}_{-54}	0.1	0.715 ± 0.008
O3b - GW191204_171526	2	1259514944.087	17.5	2.05 ± 0.05	68^{+6}_{-4}	0.3	0.36 ± 0.02
O3b - GW191215_223052	2	1260484270.995	11.2	1.69 ± 0.02	148^{+18}_{-15}	0.2	0.50 ± 0.02
O3b - GW191222_033537	2	1261020955.347	12.5	1.82 ± 0.01	272^{+55}_{-36}	≤ 0.1	0.771 ± 0.007
O3b - GW191230_180458	2	1261764316.898	14.4	1.77 ± 0.08	296^{+61}_{-40}	≤ 0.1	0.31 ± 0.04
O3b - GW200219_094415	2	1266140673.095	10.7	1.75 ± 0.07	224^{+42}_{-28}	≤ 0.1	0.28 ± 0.05
O3b - GW200224_222234	2	1266618172.381	20.0	1.74 ± 0.01	247^{+24}_{-17}	7.4	0.0017 ± 0.0005
O3b - GW200225_060421	2	1266645879.413	12.5	1.89 ± 0.04	115^{+13}_{-10}	0.7	0.21 ± 0.02
O3b - GW200311_115853	2	1267963151.380	17.8	1.80 ± 0.01	212^{+17}_{-14}	0.3	0.561 ± 0.006

detections from LVK collaboration [3–5]. The subset comprises all the BBH events that possess a network SNR greater than 10 in the cWB search for generic GWTs [39–41].[3] The selection is motivated by the reasonable expectation that the signal amplitude of echoes is such that $A \ll 1$, since no signals with amplitude comparable to that of the merger have been observed after the ringdown phase of any BBH GW emission. The list of investigated BBH events and related main results is given in Table I.

A. Robustness of cWB ES search

The BKG simulations show that the statistical properties of the noise background are weakly related to the choice of $\Delta t_{\mathrm{blind}}$ within the range $(0.05, 0.4)$ s. Therefore, any $\Delta t_{\mathrm{blind}}$ in this range can be freely selected for the cWB ES search. Instead, the noise level starts to increase as $\Delta t_{\mathrm{blind}}$ gets shorter due to some residual leakage from the primary BBH GWT signal into the PMW. The duration of the PMW window, Δt^{PMW}, affects as expected the mean $\mathrm{SNR}^{\mathrm{PMW}}$ from the BKG analysis, the longer Δt^{PMW} the larger the noise in the PMW.

We also tested the robustness of the cWB ES search against variations of the injected secondary signals in SIG analyses, see Sec. III C, for a few BBH GWT cases. By changing the delay time t_{eco} and time separation Δt_{echo} of the two pulses of the signal proxy defined in Sec. II A, the detection probability at FAP = 5% results unaffected as long as both pulses occur inside the analyzed time window, PMW. Therefore, the off-source results reported in this work can be considered valid as long as Δt^{PMW} and $\Delta t_{\mathrm{blind}}$ are included in the tested ranges, $[0.2.1.2]$ s and $[0.05, 0.2]$ s, respectively, regardless of the choice $t_{\mathrm{eco}} = \Delta t_{\mathrm{echo}} = 0.3$ s which we adopted in the SIG analyses of all BBH GWTs.

Moreover, we checked the sensitivity of the cWB ES search to widely different morphologies of postringdown signals, by performing additional SIG analyses. Figure 5 shows the DP at FAP = 5% as a function of the injected $\mathrm{SNR}^{\mathrm{PMW}}$ for different central frequencies of the SGE echo signal proxy (see Sec. II A), for a single pulse made by a BBH merger waveform and for a single burst of white noise. The resulting performances are almost identical within uncertainties, which is an expected outcome due to the general nature of the cWB search (see Sec. III A). The slight decrease in performances when injecting white noise burst signals in the PMW is mostly related to their wider frequency band.

B. Detection probability

We discuss here the detection probability measurements for the echo signal proxy described in Sec. II A, with the

---

[3]The network SNR recovered by cWB is consistent to the one recovered by template searches for these loud BBH events.
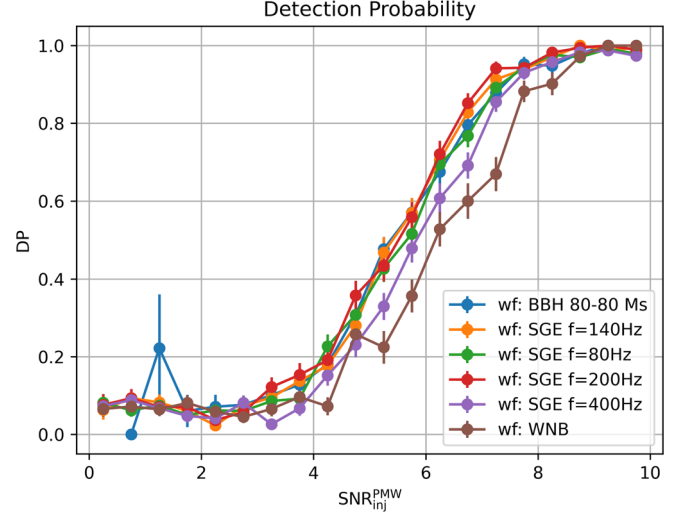

FIG. 5. DP at FAP = 5% as a function of $\mathrm{SNR}^{\mathrm{PMW}}_{\mathrm{inj}}$ for different morphologies of simulated postringdown signals: a high mass $(80 - 80 M_{\odot})$ BBH coalescence (blue), trains of two elliptically polarised sine-Gaussian pulses as described in Sec. II A with different central frequencies $f_0 = 80, 140, 200, 400$ Hz (orange, green, red, and violet, respectively) and a single pulse of white noise burst, WNB, of duration ~ 0.02 s, central frequency 150 Hz and bandwidth 100 Hz (brown). These results refer to GW150914.

requirement of FAP = 5%. Figure 6 shows the DP as a function of the h_{rss} injected inside the PMW for a subset of GWTs from the three LVK observing runs (O1, O2, O3). The visible improvement towards smaller h_{rss} comes from the temporal enhancement of the detectors' sensitivities. Between O1 and O2 observing runs, the
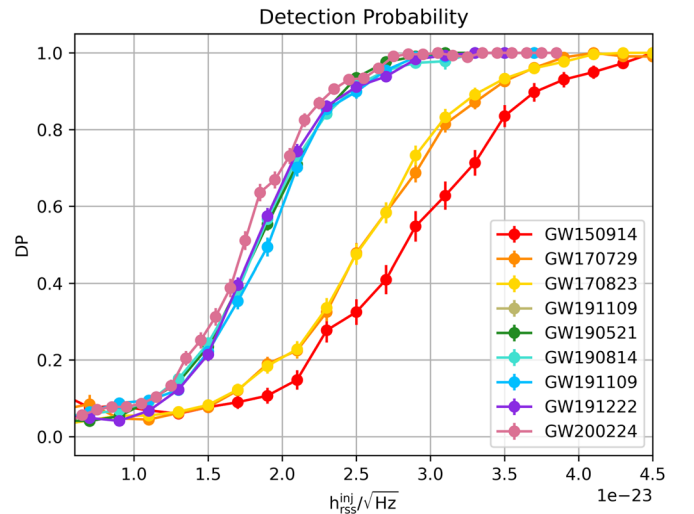

FIG. 6. Plot of the detection probability as a function of $h_{\mathrm{rss}}^{\mathrm{inj}}$ of the echo signal proxy for a selection of BBH GWTs from each observing run of the LVK (O1, O2, and O3). The $h_{\mathrm{rss}}^{\mathrm{inj}}$ units are $10^{-23} \cdot \sqrt{\mathrm{Hz}}$. The temporal sensitivity improvement achieved is visible by the shift of the curves to lower $h_{\mathrm{rss}}^{\mathrm{inj}}$.

typical h_{rss} at 50% DP decreases from $\sim 2.7 \times 10^{-23}/\sqrt{Hz}$ to $\sim 2.5 \times 10^{-23}/\sqrt{Hz}$. A more significant decrease in h_{rss} at 50% DP can be seen from O2 to O3, from average values of $\sim 2.5 \times 10^{-23}/\sqrt{Hz}$ to $\sim 1.8 \times 10^{-23}/\sqrt{Hz}$, corresponding to an improvement of about 28%. Column 6 of Table I reports the resulting h_{rss} values which ensure 50% DP with FAP 5% for all the studied GWTs.

The coherent WaveBurst ES search explores a significantly lower range of h_{rss} values with respect to the cWB all-sky search for short-duration bursts [41]. For the latter, the best results in terms of h_{rss} values at DP $= 50\%$ among the tested signal morphologies has been achieved in O3 for a single pulse SGE, $Q = 100$, $f_0 = 235$ Hz, reaching $h_{rss} = 8 \times 10^{-23}/\sqrt{Hz}$ at a FAR of one per 100 years. Here instead, with a more dispersed signal, the double pulse SGE, $Q = 8.8$, $f_0 = 140$ Hz, the average h_{rss} values at DP $= 50\%$ in O3 reaches $\sim 1.9 \times 10^{-23}/\sqrt{Hz}$, but at a much higher FAR of 2 per year, estimated by multiplying the FAP by the rate of the investigated BBH GWTs.

C. On-source *p* value

The on-source (ON) data for each BBH GWT is analyzed using the same configuration of the cWB ES search of the SIG and BKG analyses (see Sec. III C). By comparing the ON results with their BKG distributions we can estimate the p value of SNR_{ON}^{PMW} per each BBH GWT:

$$p \text{ value}_{ON} = \frac{EV_{BKG}(SNR_{rec}^{PMW} \geq SNR_{ON}^{PMW})}{EV}, \quad (11)$$

where SNR_{ON}^{PMW} is the on-source reconstructed SNR inside the PMW, EV is the total number of BKG instances and EV_{BKG} is the number of BKG instances with SNR_{rec}^{PMW} above the ON value. A low p value points to SNR_{ON}^{PMW} on the high-energy tail of the SNR_{rec}^{PMW} distribution for the null hypothesis. Columns 8 and 9 of Table I list the SNR_{ON}^{PMW} and p value$_{ON}$ per each BBH GWT. Figure 7 reports the p value for each investigated GWT, ranked from the lowest to the highest. These estimates are based on the BKG analyses performed over approximately one calendar month of data around each BBH GWT. We set an *a priori* threshold on the false discovery rate [61], FDR < 0.1, to select the p values hinting at a rejection of the null hypothesis. These cases are then the object of deeper followup studies.

Two GW events, GW190701 and GW200224, show an interesting SNR_{ON}^{PMW} and their p values pass the *a priori* FDR threshold. In both cases, the morphological information of the outliers reconstructed inside the PMW (see Appendix B) points to a dominant contribution by known instrumental disturbances in the frequency range (16,40) Hz [62,63]. These noise disturbances are known to often occur as a train of more pulses with a quasiregular time separation. This feature is especially evident in our analysis of GW200224 (see Appendix B 2) and can affect
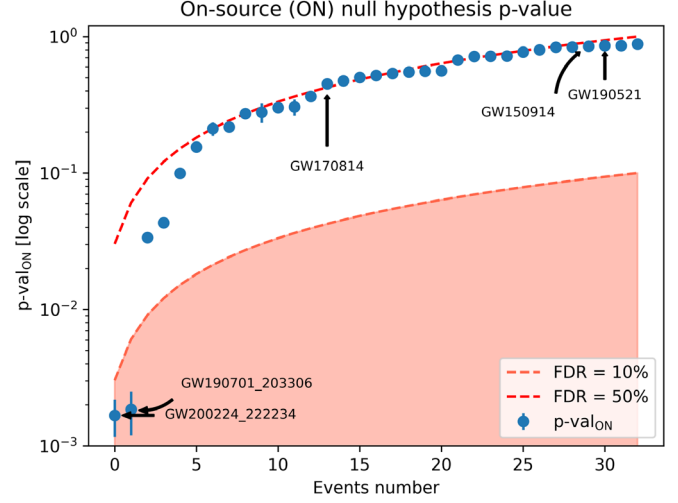

FIG. 7. The plot shows the ordered p-values of SNR_{ON}^{PMW} for the null hypothesis as measured by BKG analyses. p values and their statistical uncertainties are represented by the blue dots. The red dashed line corresponds to the expected values for the null hypothesis (FDR $= 50\%$). The orange dashed line and orange filled area corresponds to a FDR $= 10\%$, and to the region FDR $< 10\%$, respectively. This area is used to select echo candidates.

our p-value estimates, since it violates the assumption of uniformly random occurrence times and of independence of each noise pulse. Therefore, one can expect, at the very least, an underestimation of the uncertainties of our p values.

We checked for systematic errors in the p values of GW190701 and GW200224 by changing the off-source injection times of the BBH GWTs inside the BKG analysis. In particular, we repeated the BKG analysis using only 4096 s of data around the GWT time. The new local p-value estimates are

$$GW190701: \ p \text{ value}_{ON}^{local} = 0.004 \pm 0.002, \quad (12)$$

$$GW200224: \ p \text{ value}_{ON}^{local} = 0.007 \pm 0.002, \quad (13)$$

which are also reported in Fig. 11 in Appendix B. In the case of GW200224, the discrepancy between the estimates points to large systematic effects, including a significant bias of the p value, which weakens its initial statistical significance. As for GW190701, the local p-value estimate is also higher than the initial one, though it may still be compatible within the stated statistical uncertainties.

Further statistical checks and more morphological tests on GW190701 and GW 200224 are reported in Appendix B. Among these checks, the most important observation is that the reconstructed frequency spectrum for both the candidates does not match any expectation from echo models [18], so these outliers cannot be considered plausible candidates for echoes. We conclude

that these two outliers are not suitable candidates for echo signals and are very likely instrumental disturbances.

For all the other GWTs, our p-value estimates occur well above our FDR threshold of attention, and their distribution is well described by the empirical BKG model. Therefore, our work does not reject the null hypothesis, confirming what was previously reported by different search methods:

(1) the generic echo search of [24], which estimated p values in the postringdown of the GWTs detected in observing runs O1 and O2 [25] and in O3b [13]; and

(2) the template-based searches [11,12] on O1, O2 data, and [21,23], which provided p-value estimates for O1 GWTs plus GW170104.

We discuss the comparison of performances with the cWB ES search in Sec. V.

D. Upper limits on h_{rss} of echoes

The confidence belt construction procedure requires SIG analyses with extended statistics. Therefore, we prioritized the GWTs with a merger and ringdown (MR) $\mathrm{SNR}_{\mathrm{MR}} \geq 7$, as reported in [5,13], if detectable by the cWB all-sky burst search. We also added to this list the outstanding GW event GW190814 [64].

All confidence intervals result in upper limits on the h_{rss} of the echo signals, $h_{\mathrm{rss}}^{\mathrm{UL}}$ (see Table II) with the exception of GW200224 (see Sec. IV C and Appendix B 2).

Typical upper limits values are in the h_{rss} range $\sim 1 \div 4 \times 10^{-23}/\sqrt{\mathrm{Hz}}$ at 95% coverage. The results in terms of h_{rss} can be directly converted to GW strain amplitudes through Eq. (10), once a specific waveform of echo signal is assumed.

The ratios between $h_{\mathrm{rss}}^{\mathrm{UL}}$ and the merger-ringdown h_{rss} of the primary BBH GWT, $h_{\mathrm{rss}}^{\mathrm{MR}}$, are also reported in Table II. These ratios are our measured amplitude upper limits in relative terms, though their connection to the echo's A parameter (see Sec. II) depends on the actual morphologies of echo models and of the primary BBH GWT. In the approximation that the merger-ringdown and each echo pulse share similar morphologies (e.g., similar central frequency and number of cycles), then the reported h_{rss} ratios can be considered to be equivalent to upper limits on A. They are conservative upper limits in case more echo pulses are detected by cWB ES search within the PMW.

V. COMPARISON WITH PREVIOUS SEARCHES FOR ECHOES

Here we provide some comments on the performances of the cWB ES search with respect to previously reported methods, being aware, however, that a full comparison of performances would require additional coordinated simulations which are computationally costly and beyond the scope of this paper. In particular, we are not able to provide comparisons with LVK searches for echoes reported

TABLE II. List of the BBH GWTs selected for setting confidence intervals on the echo's amplitude. They are a subset of the loudest ones listed in Table I. The columns report: the GWT name; the merger-ringdown h_{rss} of the primary BBH GWT, $h_{\mathrm{rss}}^{\mathrm{MR}}$; the upper limit in terms of h_{rss} of possible echo candidates inside the PMW, $h_{\mathrm{rss}}^{\mathrm{UL}}$; the relative amplitude upper limit defined as the ratio between the $h_{\mathrm{rss}}^{\mathrm{UL}}$ and $h_{\mathrm{rss}}^{\mathrm{MR}}$.

Upper limits on echoes amplitude			
GW name	$h_{\mathrm{rss}}^{\mathrm{MR}} \cdot \frac{10^{-23}}{\sqrt{\mathrm{Hz}}}$	$h_{\mathrm{rss}}^{\mathrm{UL}} \cdot \frac{10^{-23}}{\sqrt{\mathrm{Hz}}}$	$\frac{h_{\mathrm{rss}}^{\mathrm{UL}}}{h_{\mathrm{rss}}^{\mathrm{MR}}}$
GW150914	16.0	3.4	0.21
GW170104	11.5	2.2	0.20
GW170809	11.3	2.5	0.22
GW170814	12.1	2.5	0.21
GW170823	9.8	2.5	0.26
GW190408_181802	5.5	1.7	0.31
GW190412	4.2	1.3	0.31
GW190513_205428	8.1	1.4	0.17
GW190521	14.8	2.4	0.15
GW190521_074359	15.1	2.5	0.17
GW190814	2.0	1.5	0.75
GW190828_063405	15.0	1.6	0.11
GW191109_010717	6.2	2.1	0.34
GW200225_060421	5.1	2.8	0.55
GW200311_115853	7.9	2.0	0.25
GW200224_222234[a]	10.8	3.7	0.34

[a]This GWT event is affected by a loud instrumental glitch in the PMW (see Appendix B 2).

in [11–13], because the published information on this topic is not detailed enough. Instead, a partial comparison is feasible with a few dedicated papers: we focus on a previous model-independent search using simulated data [24], and on three template-based searches [21,23,43].

A. Model-independent search method by Tsang et al. [24]

This general search method for echoes has been first tested on simulated LIGO Hanford and Livingstone detector data assuming Gaussian noise [24], and then performed a search using real data on GWTs detected in O1 and O2 [25] and in O3 [13]. In simulated Gaussian noise, Ref. [24] shows that echo signals are confidently detectable above $\mathrm{SNR} = 12$. In addition, at $\mathrm{SNR} = 8$ the false alarm probability of noise fluctuations misidentified as signals is at the level of a few %. The comparison with our cWB ES search can only be semiquantitative since no information about the detection efficiency as a function of echo parameters is available in [24,25]. We can point out that for the cWB ES search on real data around GW150914 (HL detectors network), a signal delivering $\mathrm{SNR}^{\mathrm{PMW}} = 12$ would also ensure a very confident

detection, with a measured 100% detection probability at false alarm probability as low as our measurement limit, 0.1%. Moreover, with $\mathrm{SNR^{PMW}} = 8$ at the selected false alarm probability of 5%, the detection probability of cWB ES ranges from 95% to 99% depending on the statistics of noise outliers in different periods of observation. This means that cWB ES achieves high detection performances also at $\mathrm{SNR^{PMW}} = 8$ in real noise. Moreover, our off-source simulations clearly show that the data are not compliant with a stationary Gaussian noise model in the low SNR range of interest in the proximity of most BBH GWTs.

B. Model-dependent search method
by Lo *et al.* [23]

This has been the first model-dependent search that challenged the claim of an echo discovery after GW150914 by Abedi [20]. Figure 4 from [23] shows that an A parameter greater than 0.3 can be detected with a 5σ threshold for the GW150914 emission in Gaussian noise and using Advanced LIGO design sensitivity. The signal model's parameters used in [23] for this result are very similar to the ones used here: the only non-negligible differences are on γ parameter and number of pulses. In [23], three echolike pulses have been injected with $\gamma \sim 0.9$, while here we injected two with $\gamma = 0.5$. Detectability of $A \sim 0.3$ is well in the ballpark of our method when using real data, see last column from Table II. In particular, for GW150914, our search constrains A below 0.21 with 95% confidence. Moreover, Fig. 4 shows that cWB ES search can identify echo signals at 95% confidence when $\mathrm{SNR^{PMW}_{rec}}$ passes the 4σ threshold, a performance which is comparable with what reported in Table 3 from [23].[4]

C. Model-dependent search method
by Westerweck *et al.* [21]

This template-based search has been deployed on real data analyzing four BBH GWTs (including GW150914) and does not find violations of the null hypothesis. It estimates the p values of results by using different noise instantiations close to the GWTs times, which is a similar method to our BKG analysis. Instead, the sensitivity of this search is assessed by injecting echo waveforms on simulated Gaussian noise which preserves the actual power spectral density of the LIGO detectors at the GWTs detections. Figures 2 and 5 in [21] show that peak amplitudes of echoes detach from the noise fluctuations starting from $h_\mathrm{p} \simeq 2 \times 10^{-22}$. In actual noise, our search achieves 50% detection probability with a false alarm

probability of 5% for a peak amplitude of the assumed echo waveform $h_\mathrm{p} \sim 2.3 \times 10^{-22}$ for GW150914, as estimated from our more general result in terms of $h_\mathrm{rss50\%}$ (see Table I). Therefore, we conclude that the sensitivity of the cWB ES search is at least competitive to that of this template-based search on this specific echo model. We remark that the implementation of the model-dependent search uses a template bank and requires subtraction of the detected GWT trigger from data prior to matched filtering for the template bank. Such steps add complexity with respect to the cWB ES search.

D. Model-dependent analysis by Abedi [43]

Another systematic search for a specific echo model has been very recently reported by Abedi [43]. This search analyses 65 GWTs from the LVK catalog of compact binary coalescences. The method assumes Gaussian noise close to each GW event. The main result reported is an upper limit value to the echo amplitude, A, resulting to be $A \leq 0.42$ with a 90% credible interval, under the assumption that A is equal for all analyzed events. In addition, the Bayes factor reported for GW190521 stands out as an outlier, suggesting a preference for postmerger echoes rather than the null hypothesis. In our study, GW190521 shows an on-source p value equal to 0.569 ± 0.006, suggesting that the data in the PMW are compatible with noise. Moreover, our relative upper limit on the amplitude h_rss ratio at 95% coverage is 0.23 for GW190521 and is as low as 0.13 for the loudest GWTs.

VI. CONCLUSIONS

This paper describes a search for secondary gravitational wave transients of generic morphology which may occur shortly after the ringdown phase of a primary signal from a compact binary coalescence. The analysis method is developed on top of the coherent WaveBurst pipeline: it uses the primary GWT as a trigger and follows up the coherent response of the interferometric gravitational wave detectors on a selectable time window, defined with respect to the merger time.

The scientific motivation for this work is the search for gravitational wave echoes after binary black hole mergers. Such echoes are expected if the final remnant object is not a standard black hole from the general relativity theory, either because the event horizon is not fully absorbing or because the remnant is an exotic compact object larger than the wouldbe event horizon. The detection performances of the current search are described in terms of h_rss strain amplitude and are rather independent of the signal waveform and spectra within a wide signal class. Therefore, as long as any echo pulse occurs inside the selected time window, from 0.05 to 0.35 s or from 0.2 to 1.2 s after the merger, the

---

[4]In Table 3 of [23], the threshold on the detection statistics, which corresponds to 4σ in Gaussian noise, is delivering a 2σ confidence in real GW150914 noise, similarly to our result.

reported results can be interpreted in terms of any echoes' model.

The analysis of the loudest 33 BBH mergers detected during the O1, O2, and O3 observing runs by the LIGO, Virgo, and KAGRA collaborations is consistent with null results (see Table I), so no evidence of echo signals is found. This search provides separate results for single BBH mergers. The off-source characterization of the detection efficiency vs false alarm probability and the estimation of p values of candidates is performed using thousands of real detector noise instantiations. Therefore, the results do not rely on an *a priori* noise model and point out that the actual noise statistic is far from Gaussian in most cases, even at low SNR. The search also provides a morphological reconstruction of candidates and, for the first time, the confidence intervals on the h_{rss} amplitude of gravitational wave echoes. The latter turn out to be upper limits, typically ranging in the interval $\sim 1 \div 4 \times 10^{-23}/\sqrt{Hz}$ in terms of h_{rss} (see Table II).

The two loudest candidates found occur after GW190701 and GW200224. These candidates are also the only ones featuring low enough p values to require further followup investigations. Their morphological reconstruction clearly points to the dominating presence of known pulsating instrumental noise disturbances at low frequencies, occurring in both the LIGO detectors, and they are by far inconsistent with any published model of echoes. The pseudoregular cadence of these disturbances is the likely cause of a systematic error in our initial p-value estimates.

To our knowledge, this search for echoes is delivering the highest sensitivity to the possible presence of gravitational wave echoes occurring within a selected postmerger time window, without relying on signal templates. Our *a posteriori* use of morphological information to reject or accept candidates is still a suboptimal strategy. An *a priori* exploitation of loose morphological priors of echo signals will likely improve the current method.

We plan to extend this method also to investigate the postmerger emission after binary neutron star (BNS, see e.g., [65]) and neuron star-black hole (NSBH) coalescence over a wider frequency range, exploiting the entire spectral sensitivity of the LVK detectors. Remarkably, this search can be adapted to study other science cases of interest in current GW astronomy, which share the expectation of a weak GW feature close to the coalescence time of the primary CBC GWT signal. Examples include investigation of memory effects [66–70], precursors to highly eccentric BBHs [71–75], or microlensing effects [76,77].

ACKNOWLEDGMENTS

APPENDIX A: CWB ALL-SKY BURST SEARCH VS ES SEARCH

Table III lists cWB [37,38] parameters (first column) and their threshold values that can be tuned in a cWB search, comparing the configuration for the cWB all-sky burst search [39–41] (second column) to that of the cWB ES search (third column). The different tuning of η_c, T_{gap}, and SUBRHO thresholds is motivated by the need to grasp lower SNR triggers in the search for echoes, while keeping under control the false alarms. Additional configuration parameters are defined in the cWB ES search: the time width of the PMW, Δt^{PMW}; a blind time after the

TABLE III.   Comparison of the cWB main production thresholds between all-sky burst search [41] (second column) and ES search (third column).

Configuration parameters		
Parameters	All-sky O3 search	ES search
bpp	0.001	0.001
Subnet	0.5	0.5
c_c	0.5	0.5
η_c	5.0	3.5
A_{core}	1.7	1.7
T_{gap}	0.2 s	2.0 s
F_{gap}	128.0 Hz	128.0 Hz
SUBRHO	5.5	3.5
SUBNET	0.1	0.1
PMW	not used	$\Delta t^{PMW} = 1$ s
t_{blind}	not used	$t_{blind} \geq 40$ ms
c_c^{PMW}	not used	$c_c^{PMW} \geq 0.5$

coalescence time, t_{blind}; the fraction of correlated energy in the PMW, c_c^{PMW}.

## APPENDIX B: FOLLOWUP OF LOUDEST CANDIDATES

From the analysis of the p values of the BBH GWTs (see Sec. IV C), two events are selected for deeper investigations since they are consistent with a FDR $\leq 10\%$: GW190701 and GW200224. Estimating the p values on a different, more local set of noise instantiations results in higher p values, which points to some systematic bias in our estimating procedure. Nevertheless, these two local p values are still the only ones $\leq 1\%$, further motivating the following deeper investigations on GW190701 and GW200224.

The morphological study of the PMW on-source event allows us to gather information about the reconstructed SNR of the energy excess, its arrival time, mean frequency, and the reconstructed waveform. Additional tests have been deployed as well, like performing a single detector analysis of the on-source morphology, with the subtraction of the primary BBH waveform. The information of the morphological studies are then compared with the theoretical expectation of echo models (see Sec. II) and with the known noise disturbances.
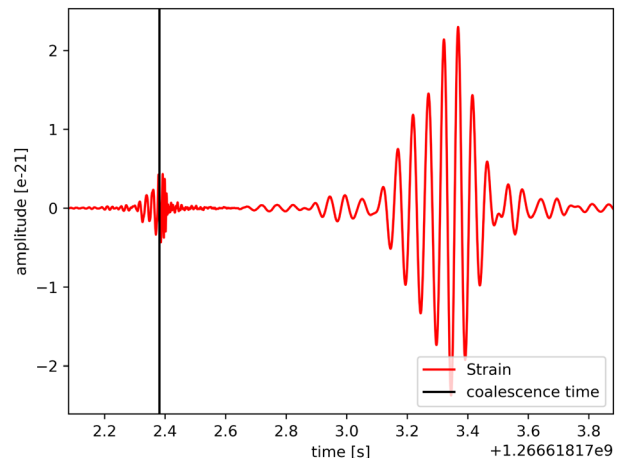
1. GW190701

Figure 8(a), shows the reconstructed strain signal waveform of GW190701 in L1 detector. Here, the BBH signal is the smallest bump on the left while the two bumps on its right are the postmerger energy excesses. Among them, the most interesting one is the second (at time ~ 168.86 s) since it is the one falling inside our PMW. The postmerger candidate shows higher strain, and longer time duration, around ≥ 100 ms, with respect to the BBH event, and no echo models are consistent, to our knowledge, with these features.

The entire on-source event (BBH + PM signals) has an overall SNR content around SNR ~ 12.9 with a $\rho \sim 4.8$, and $c_c \sim 0.57$ that is an unusually low value for an event with such an SNR. Figures 9(a) and 9(b), the two TF maps of the event for each detector, show that, in the L1 detector, after the BBH event, there are three postmerger energy excesses, at times ~ 168.64 s, ~ 168.86 s, and 169.07 s, while in the postmerger of H1 there is only one clear energy excess at ~ 168.84 s. This energy distribution asymmetry explains the low value of the correlation coefficient c_c suggesting that a noise realization is a preferred explanation for such an observation since it does not match up with echo signal predictions. Furthermore, in the bottom row of Fig. 9 there is the network on-source likelihood 9d TF map. At time ~ 168.55 s there is the chirping cluster of pixels representing the GW190701 event, going from frequencies around ~ 40 Hz up to ~ 150 Hz, while in the postmerger, at the time ~ 168.84 s, is clearly visible the energy excess. It has a
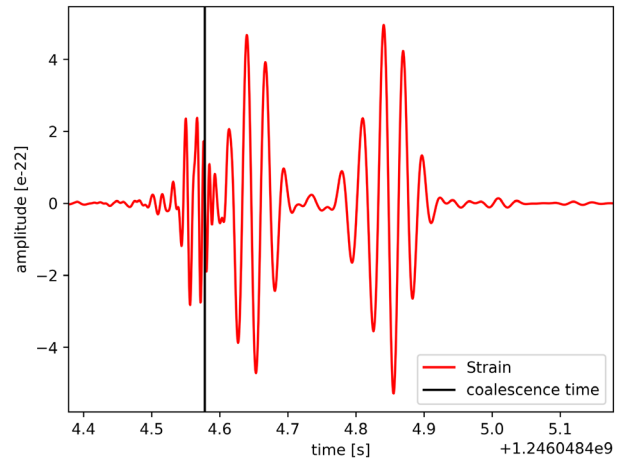
(a) GW190701 - L1 strain.

(b) GW200224 - L1 strain.

FIG. 8. Panel (a) shows the strain amplitude waveform of GW190701 and its postmerger as function of time for L1 detector. Panel (b) reports the strain amplitude of GW200224 and its postmerger as function of time for L1 detector. In both plots the black vertical line marks the coalescence time of the binary. For both the GW signals are clearly visible the glitches providing the energy excesses when running the ES search.

central frequency around $f_0 \sim [30\text{--}40]$ Hz which is not a frequency range expected for echoes: they should possess similar frequencies or higher than the BBH merger one [18]. Finally, Fig. 9(e) shows the on-source likelihood TF map after the BBH subtraction for the single L1 detector configuration. A repetition of similar pulses is visible both before and after GW190701 coalescence time (~ 168.55 s). This is again inconsistent with echo models, and points to an accidental coincidence with noisy features polluting L1 data.

2. GW200224

To study the postmerger on-source energy excess detected in GW200224 we deploy the same strategy in GW190701. Figure 8(b) shows the on-source strain waveform of the entire event, with the BBH being the small

(a) L1 TF map.

(b) H1 TF map.

(c) L1 TF map - BBH sub.

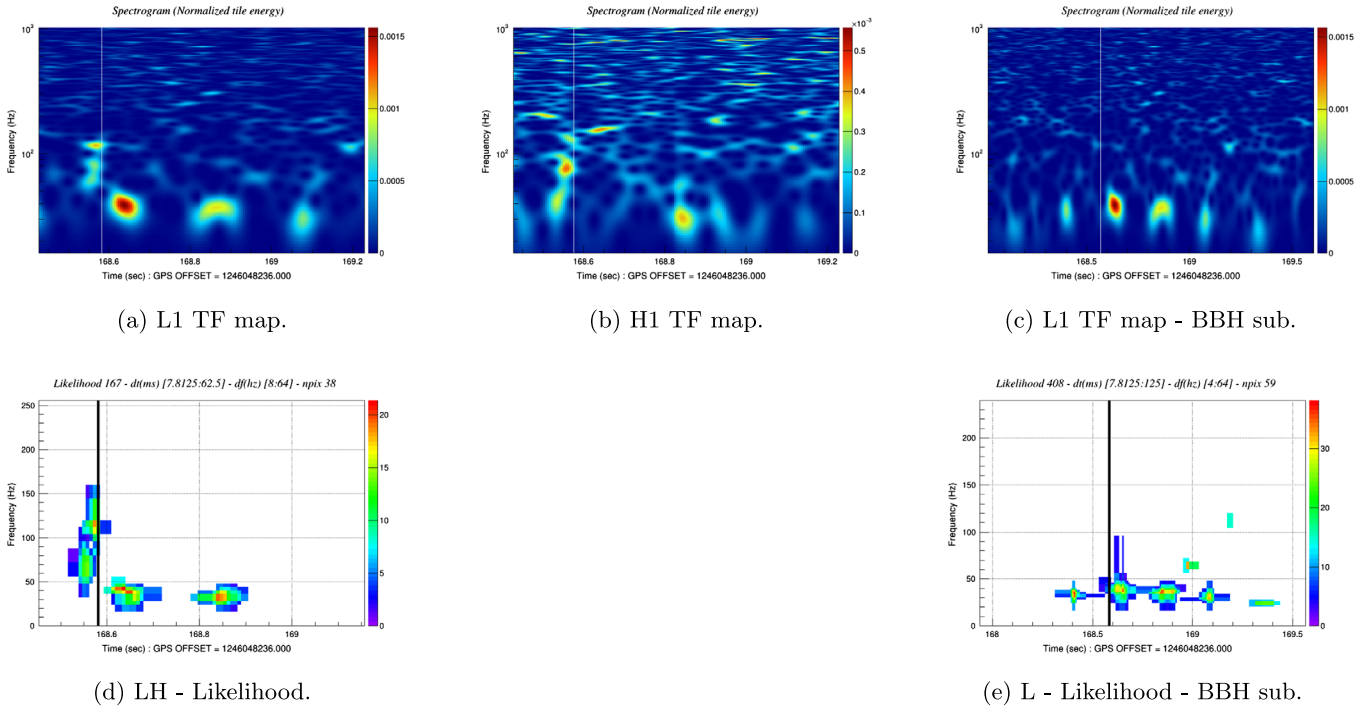(d) LH - Likelihood.

(e) L - Likelihood - BBH sub.

FIG. 9.   Plots (a) and (b) show the time-frequency map of GW190701 event in L1 and H1 detector, respectively. Plot (c) shows the event in L1 detector once the best template of GW190701 between its posterior samples is subtracted from the data. The white vertical line marks the coalescence time of the BBH event. Plot (d) shows the reconstructed maximum likelihood of the event for the LH network, while plot (e) displays the same quantity but for a single detector search (L1) and after the best GW190701 template is subtracted from the data. The black vertical line marks the coalescence time of the BBH event. Note that the color bars scale between L and H detectors have a different range.

(a) L1 TF map.

(b) H1 TF map.

(c) L1 TF map - BBH sub.

(d) LH - Likelihood.

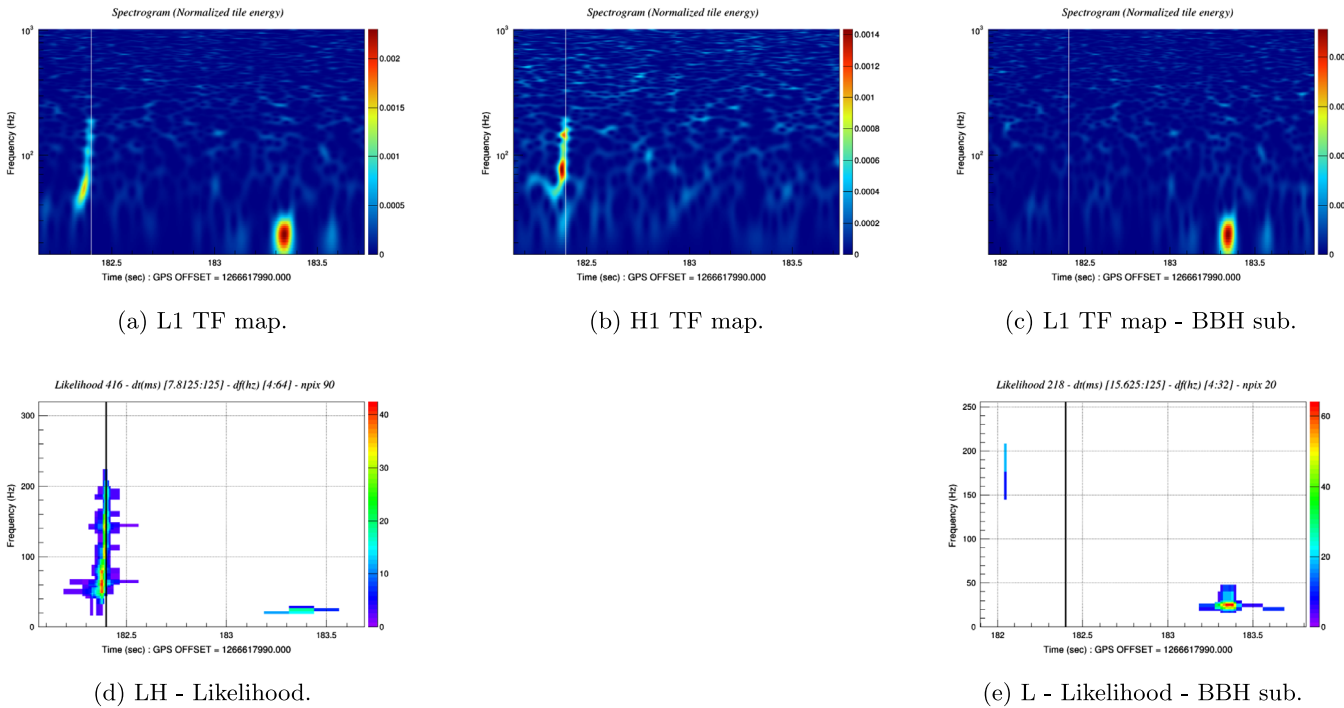(e) L - Likelihood - BBH sub.

FIG. 10.   Plots (a) and (b) show the time-frequency map of GW200224 event in L1 and H1 detector, respectively. Plot (c) shows the event in L1 detector once the best template of GW200224 between its posterior samples is subtracted from the data. The white vertical line marks the coalescence time of the BBH event. Plot (d) show the reconstructed maximum likelihood of the event for the LH network, while plot (e) display the same quantity but for a single detector search (L1) and after the best GW200224 template is subtracted from the data. The black vertical line marks the coalescence time of the BBH event. Note that the color bars scale between L and H detectors have a different range.

signal on the left. The time duration of the PM signal, ~ 400 ms as well as its time distance of ~ 1 s to the merger time of the BBH do not match the theoretical predictions of echo signals. Following Eq. (3) t_{echo} is predicted to be $\sim$ms after t_{coa}. Moreover, the TF map of the on-source event, Fig. 10(a) shows that the mean frequency of this PM excess of energy is around 40 Hz well below the expected frequency values for echoes.

Figures 10(a) and 10(b), the TF maps of the event in L1 and H1, respectively, shows that the PM signal is present only in L1 detector, while in H1 such high energy excess is not reconstructed. Since the two LIGO detectors are nearly aligned and are sensitive to the same GW's polarization, for real astrophysical events such energy imbalance in the detectors is suspicious.

We proceed in subtracting to GW200224 on-source event the best PE model describing that same BBH event, then on the subtracted data we run the single detector ES search. The result is displayed in Fig. 10(e). Here, no undetected energy excess other than the investigated one appears, suggesting that we are not in a scenario similar to the single detector analysis of GW190701. The energy outlier has a SNR ~ 10.4, while the overall SNR of the BBH signal plus postmerger excess of energy is equal to ~ 16.8 (in single detector mode).

3. cWB ES search with 32 Hz mitigation

The PMW on-source morphologies hint to a possible data pollution by a glitch family identified in the frequency range $\in (16, 40)$ Hz [62,63]. Therefore, we repeated the ES search for these two GWTs by including a specific single detector data filter [78,79] that estimates the power oscillations within the frequency range $\in (16 - 40)$ Hz and attenuates them. We label such analysis as 32 Hz-ES search, to differentiate it from the standard ES search. The measured on-source null hypothesis p values when the noise around 32 Hz frequencies is mitigated result:

$$\text{GW190701: } p\,\text{value}_{\text{ON}}^{32\,\text{Hz}} = 0.024 \pm 0.002, \quad \text{(B1)}$$
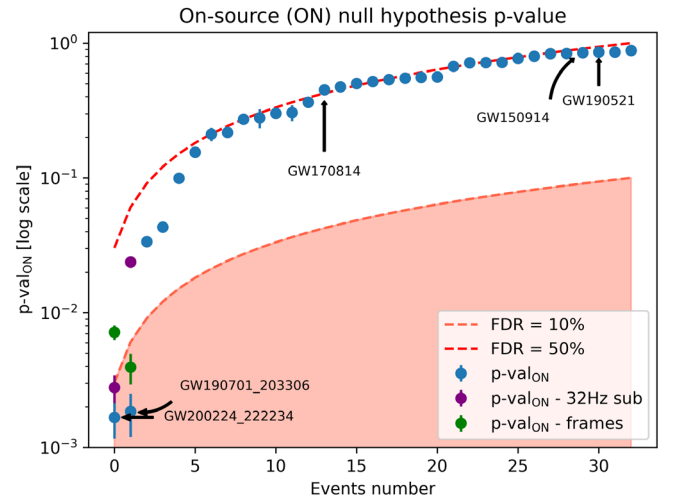

FIG. 11. Same plot of Fig. 7, where the green dots are the on-source p value obtained from the ES search carried on using only the 4096 s around the main BBH event. The violet dots are the on-source p value for the ES search performed over the same standard analysis data but applying a 32 Hz data mitigation plugin to suppress some noisy contaminating the O3a and O3b observational periods.

$$\text{GW200224: } p\,\text{value}_{\text{ON}}^{32\,\text{Hz}} = 0.003 \pm 0.001 \quad \text{(B2)}$$

and they are plotted in Fig. 11 as the violet dots. This noise mitigation rules out the postmerger event candidate GW190701, while for the PM of GW200224 the p value is still within the FRD $\leq 10\%$.

This study together with the morphological investigation of the PMW energy excesses of GW190701 and GW200224 (see Appendices B 1 and B 2), show that it is reasonable to assume them to be nonstationary noise feature polluting the data and especially affecting L detector. These noise transients posses a central frequency around (30,40) Hz, and have a greater time duration ($\sim$ hundred of ms) with respect to the expected one for echo signals ($\sim$ tens of ms), so around one order of magnitude bigger.

[1] The LIGO Scientific Collaboration, Advanced LIGO, Classical Quantum Gravity **32**, 074001 (2015).
[2] The Virgo Scientific Collaboration, Advanced Virgo: A second-generation interferometric gravitational wave detector, Classical Quantum Gravity **32**, 024001 (2014).
[3] B. P. Abbott *et al.* (LIGO Scientific and Virgo Collaborations), GWTC-1: A Gravitational-Wave Transient Catalog of Compact Binary Mergers Observed by LIGO and Virgo during the First and Second Observing Runs, Phys. Rev. X **9**, 031040 (2019).
[4] R. Abbott *et al.* (LIGO Scientific and Virgo Collaborations), GWTC-2: Compact Binary Coalescences Observed by LIGO and Virgo during the First Half of the Third Observing Run, Phys. Rev. X **11**, 021053 (2021).
[5] R. Abbott *et al.* (LIGO Scientific, Virgo, and KAGRA Collaborations), GWTC-3: Compact binary coalescences observed by LIGO and Virgo during the second part of the third observing run, arXiv:2111.03606.

[6] KAGRA Scientific Collaboration, KAGRA: 2.5 generation interferometric gravitational wave detector, Nat. Astron. **3,** 35 (2019).

[7] The LIGO Collaboration, The gravitational-wave candidate event database (GraceDB), https://gracedb.ligo.org/.

[8] W. G. Unruh and R. M. Wald, Information loss, Rep. Prog. Phys. **80,** 092002 (2017).

[9] A. Einstein, Die Grundlage der allgemeinen Relativitätstheorie, Ann. Phys. (Berlin) **354,** 769 (1916).

[10] B. P. Abbott *et al.* (LIGO Scientific and Virgo Collaborations), Tests of General Relativity with GW150914, Phys. Rev. Lett. **116,** 221101 (2016).

[11] R. Abbott *et al.* (LIGO Scientific and Virgo Collaborations), Tests of general relativity with the binary black hole signals from the LIGO-Virgo catalog GWTC-1, Phys. Rev. D **100,** 104036 (2019).

[12] R. Abbott *et al.* (LIGO Scientific and Virgo Collaborations), Tests of general relativity with binary black holes from the second LIGO-Virgo gravitational-wave transient catalog, Phys. Rev. D **103,** 122002 (2021).

[13] R. Abbott *et al.* (LIGO Scientific, Virgo, and KAGRA Collaborations), Tests of General Relativity with GWTC-3, arXiv:2111.03606 [Phys. Rev. X (to be published)].

[14] A. Testa and P. Pani, Analytical template for gravitationalwave echoes: Signal characterization and prospects of detection with current and future interferometers, Phys. Rev. D **98,** 044018 (2018).

[15] E. Maggio, A. Testa, S. Bhagwat, and P. Pani, Analytical model for gravitational-wave echoes from spinning remnants, Phys. Rev. D **100,** 064056 (2019).

[16] V. Cardoso, E. Franzin, and P. Pani, Is the GravitationalWave Ringdown a Probe of the Event Horizon?, Phys. Rev. Lett. **116,** 171101 (2016).

[17] V. Cardoso, S. Hopper, C. F. B. Macedo, C. Palenzuela, and P. Pani, Gravitational-wave signatures of exotic compact objects and of quantum corrections at the horizon scale, Phys. Rev. D **94,** 084031 (2016).

[18] Q. Wang and N. Afshordi, Black hole echology: The observer's manual, Phys. Rev. D **97,** 124044 (2018).

[19] Z. Mark, A. Zimmerman, S. M. Du, and Y. Chen, A recipe for echoes from exotic compact objects, Phys. Rev. D **96,** 084002 (2017).

[20] J. Abedi, H. Dykaar, and N. Afshordi, Echoes from the abyss: Tentative evidence for Planck-scale structure at black hole horizons, Phys. Rev. D **96,** 082004 (2017).

[21] J. Westerweck, A. B. Nielsen, O. Fischer-Birnholtz, M. Cabero, C. Capano, T. Dent, B. Krishnan, G. Meadors, and A. H. Nitz, Low significance of evidence for black hole echoes in gravitational wave data, Phys. Rev. D **97,** 124037 (2018).

[22] A. B. Nielsen, C. D. Capano, O. Birnholtz, and J. Westerweck, Parameter estimation and statistical significance of echoes following black hole signals in the first Advanced LIGO observing run, Phys. Rev. D **99,** 104012 (2019).

[23] R. K. L. Lo, T. G. F. Li, and A. J. Weinstein, Templatebased gravitational-wave echoes search using Bayesian model selection, Phys. Rev. D **99,** 084052 (2019).

[24] K. W. Tsang, A. Ghosh, A. Samajdar, M. Agathos, K. Chatziioannou, V. Cardoso, G. Khanna, and C. Van Den Broeck, A morphology-independent data analysis method for detecting and characterizing gravitational wave echoes, Phys. Rev. D **98,** 024023 (2018).

[25] K. W. Tsang, A. Ghosh, A. Samajdar, K. Chatziioannou, S. Mastrogiovanni, M. Agathos, and C. Van Den Broeck, A morphology-independent search for gravitational wave echoes in data from the first and second observing runs of Advanced LIGO and Advanced Virgo, Phys. Rev. D **101,** 064012 (2020).

[26] V. Cardoso and P. Pani, Tests for the existence of black holes through gravitational wave echoes, Nat. Astron. **1,** 586 (2017).

[27] M. S. Morris, K. S. Thorne, and U. Yurtsever, Wormholes, Time Machines, and the Weak Energy Condition, Phys. Rev. Lett. **61,** 1446 (1988).

[28] F. E. Schunck and E. W. Mielke, General relativistic boson stars, Classical Quantum Gravity **20,** R301 (2003).

[29] P. O. Mazur *et al.*, Gravitational vacuum condensate stars, Proc. Natl. Astron. Soc. U.S.A. **101,** 9545 (2004).

[30] S. D. Mathur, The fuzzball proposal for black holes: An elementary review, Prog. Phys. **57,** 793 (2005).

[31] W. Rindler, Visual horizons in world models, Mon. Not. R. Astron. Soc. **116,** 662 (1956).

[32] Q. Wang, N. Oshita, and N. Afshordi, Echoes from quantum black holes, Phys. Rev. D **101,** 024031 (2020).

[33] A. Miani, Agnostic method to detect low energetic signals nearby a gravitational wave transient from a binary black hole system, 10.15168/11572-354941.

[34] S. Klimenko *et al.*, Method for detection and reconstruction of gravitational wave transients with networks of advanced detectors, Phys. Rev. D **93,** 042004 (2016).

[35] S. Klimenko, I. Yakushin, A. Mercer, and G. Mitselmakher, A coherent method for detection of gravitational wave bursts, Classical Quantum Gravity **25,** 114029 (2008).

[36] S. Klimenko, S. Mohanty, M. Rakhmanov, and G. Mitselmakher, Constraint likelihood analysis for a network of gravitational wave detectors, Phys. Rev. D **72,** 122002 (2005).

[37] M. Drago *et al.*, Coherent WaveBurst, A pipeline for unmodeled gravitational-wave data analysis, SoftwareX **14,** 100678 (2021).

[38] Coherent WaveBurst group, https://gwburst.gitlab.io/ (2003).

[39] B. P. Abbott *et al.* (LIGO Scientific and Virgo Collaborations), All-sky search for short gravitational-wave bursts in the first Advanced LIGO run, Phys. Rev. D **95,** 042003 (2017).

[40] B. P. Abbott *et al.* (LIGO Scientific and Virgo Collaborations), All-sky search for short gravitational-wave bursts in the second Advanced LIGO and Advanced Virgo run, Phys. Rev. D **100,** 024017 (2019).

[41] R. Abbott *et al.* (LIGO Scientific Collaboration, Virgo Collaboration, and KAGRA Collaboration), All-sky search for short gravitational-wave bursts in the third Advanced LIGO and Advanced Virgo run, Phys. Rev. D **104,** 122004 (2021).

[42] P. J. Sutton, A rule of thumb for the detectability of gravitational-wave bursts, arXiv:1304.0210.

[43] Jahed Abedi, Search for echoes on the edge of quantum black holes, arXiv:2301.00025.

[44] V. Cardoso, L. C. B. Crispino, C. F. B. Macedo, H. Okawa, and P. Pani, Light rings as observational evidence for event horizons: Long-lived modes, ergoregions and nonlinear instabilities of ultracompact objects, Phys. Rev. D **90,** 044069 (2014).

[45] V. Ferrari and K. D. Kokkotas, Scattering of particles by neutron stars: Time evolutions for axial perturbations, Phys. Rev. D **62,** 107504 (2000).

[46] A. Maselli, S. H. Völkel, and K. D. Kokkotas, Parameter estimation of gravitational wave echoes from exotic compact objects, Phys. Rev. D **96,** 064045 (2017).

[47] J. Abadie *et al.* (The LIGO Scientific and The Virgo Collaborations), All-sky search for gravitational-wave bursts in the second joint LIGO-Virgo run, Phys. Rev. D **85,** 122007 (2012).

[48] The LIGO Scientific Collaboration, https://www.ligo.org/.

[49] The Virgo Collaboration, https://www.virgo-gw.eu/.

[50] The KAGRA Collaboration, https://gwcenter.icrr.u-tokyo.ac .jp/en/.

[51] S. Chatterji, A. Lazzarini, L. Stein, P. J. Sutton, A. Searle, and M. Tinto, Coherent network analysis technique for discriminating gravitational-wave bursts from instrumental noise, Phys. Rev. D **74,** 082005 (2006).

[52] F. Salemi, E. Milotti, G. A. Prodi, G. Vedovato, C. Lazzaro, S. Tiwari, S. Vinciguerra, M. Drago, and S. Klimenko, Wider look at the gravitational-wave transients from GWTC-1 using an unmodeled reconstruction method, Phys. Rev. D **100,** 042003 (2019).

[53] Coherent WaveBurst group, The whitening, https://gwburst .gitlab.io/documentation/latest/html/faq.html.

[54] R. Abbott *et al.* (LIGO Scientific, Virgo, and KAGRA Collaborations), Open data from the first and second observing runs of Advanced LIGO and Advanced Virgo, SoftwareX **13,** 100658 (2021).

[55] R. Abbott *et al.* (LIGO Scientific, Virgo, and KAGRA Collaborations), Open data from the third observing run of LIGO, Virgo, KAGRA and GEO, arXiv:2302.03676.

[56] B. P. Abbott *et al.* (LIGO Scientific and Virgo Collaborations), Observation of Gravitational Waves from a Binary Black Hole Merger, Phys. Rev. Lett. **116,** 061102 (2016).

[57] B. P. Abbott *et al.* (LIGO Scientific and Virgo Collaborations), Observing gravitational-wave transient GW150914 with minimal assumptions, Phys. Rev. D **93,** 122004 (2016).

[58] B. P. Abbott *et al.* (LIGO Scientific and Virgo Collaborations), Properties of the Binary Black Hole Merger GW150914, Phys. Rev. Lett. **116,** 241102 (2016).

[59] R. Abbott *et al.* (LIGO Scientific and Virgo Collaborations), GW190521: A Binary Black Hole Merger with a Total Mass of $150 M_\odot$, Phys. Rev. Lett. **125,** 101102 (2020).

[60] J. Neyman, Outline of a theory of statistical estimation based on the classical theory of probabilitye, Phil. Trans. R. Soc. A **236,** 333 (1937).

[61] C. J. Miller, C. Genovese, R. C. Nichol, L. Wasserman, A. Connolly, D. Reichart, A. Hopkins, J. Schneider, and A. Moore, Controlling the false-discovery rate in astrophysical data analysis, Astron. J. **122,** 3492 (2001).

[62] M. Cabero *et al.*, Blip glitches in Advanced LIGO data, Classical Quantum Gravity **36,** 155010 (2019).

[63] B. P. Abbott *et al.* (The LIGO Scientific and The Virgo Collaborations), Effects of data quality vetoes on a search for compact binary coalescences in Advanced LIGO's first observing run, Classical Quantum Gravity **35,** 065010 (2018).

[64] R. Abbott *et al.* (LIGO Scientific and Virgo Collaborations), GW190814: Gravitational waves from the coalescence of a 23 solar mass black hole with a 2.6 solar mass compact object, Astrophys. J. Lett. **896,** L44 (2020).

[65] B. P. Abbott *et al.* (LIGO Scientific and Virgo Collaborations), GW170817: Observation of Gravitational Waves from a Binary Neutron Star Inspiral, Phys. Rev. Lett. **119,** 161101 (2017).

[66] D. Christodoulou, Nonlinear Nature of Gravitation and Gravitational-Wave Experiments, Phys. Rev. Lett. **67,** 1486 (1991).

[67] M. Favata, The gravitational-wave memory effect, Classical Quantum Gravity **27,** 084036 (2010).

[68] M. Hübner, C. Talbot, P. D. Lasky, and E. Thrane, Measuring gravitational-wave memory in the first LIGO/Virgo gravitational-wave transient catalog, Phys. Rev. D **101,** 023011 (2020).

[69] M. Hübner, P. Lasky, and E. Thrane, Memory remains undetected: Updates from the second LIGO/Virgo gravitational-wave transient catalog, Phys. Rev. D **104,** 023004 (2021).

[70] S. Tiwari, M. Ebersold, and E. Z. Hamilton, Leveraging gravitational-wave memory to distinguish neutron star-black hole binaries from black hole binaries, Phys. Rev. D **104,** 123024 (2021).

[71] Y. Setyawati and F. Ohme, Adding eccentricity to quasi-circular binary-black-hole waveform models, Phys. Rev. D **103,** 124011 (2021).

[72] M. Ebersold and S. Tiwari, Search for nonlinear memory from subsolar mass compact binary mergers, Phys. Rev. D **101,** 104041 (2020).

[73] B. P. Abbott *et al.* (LIGO Scientific and Virgo Collaborations), Search for eccentric binary black hole mergers with Advanced LIGO and Advanced Virgo during their first and second observing runs, Astrophys. J. **883,** 149 (2019).

[74] R. Gamba, M. Breschi, G. Carullo, S. Albanesi, P. Rettegno, S. Bernuzzi, and A. Nagar, GW190521 as a dynamical capture of two nonspinning black holes, Nat. Astron. **7,** 11 (2022).

[75] M. Ebersold, S. Tiwari, L. Smith, Y.-B. Bae, G. Kang, D. Williams, A. Gopakumar, I. S. Heng, and M. Haney, Observational limits on the rate of radiation-driven binary black hole capture events, Phys. Rev. D **106,** 104014 (2022).

[76] J. M. Ezquiaga, D. E. Holz, W. Hu, M. Lagos, and R. M. Wald, Phase effects from strong gravitational lensing of gravitational waves, Phys. Rev. D **103,** 064047 (2021).

[77] R. Abbott *et al.*, Search for lensing signatures in the gravitational-wave observations from the first half of LIGO–Virgo's third observing run, Astrophys. J. **923,** 14 (2021).

[78] M. Szczepańczyk *et al.*, Observing an intermediate-mass black hole GW190521 with minimal assumptions, Phys. Rev. D **103,** 082002 (2021).

[79] V. Tiwari *et al.*, Regression of environmental noise in LIGO data, Classical Quantum Gravity **32,** 165014 (2015).